

**Shining Light on Dark Matter,
One Photon at a Time**

by

Brandon Leigh Allen

Submitted to the Department of Physics
in partial fulfillment of the requirements for the degree of

Doctorate of Science in Physics

at the

MASSACHUSETTS INSTITUTE OF TECHNOLOGY

June 2019

© Massachusetts Institute of Technology 2019. All rights reserved.

Author
Department of Physics
May 18, 2019

Certified by
Christoph E.M. Paus
Professor
Thesis Supervisor

Accepted by
Nergis Mavalvala
Associate Department Head for Education

**Shining Light on Dark Matter,
One Photon at a Time**

by

Brandon Leigh Allen

Submitted to the Department of Physics
on May 18, 2019, in partial fulfillment of the
requirements for the degree of
Doctorate of Science in Physics

Abstract

A search is conducted for new physics in final states containing a photon and missing transverse momentum in proton-proton collisions at $\sqrt{s} = 13$ TeV. The data collected by the CMS experiment at the CERN LHC correspond to an integrated luminosity of 35.9 inverse femtobarns. No deviations from the predictions of the standard model are observed. The results are interpreted in the context of dark matter production and limits on new physics parameters are calculated at 95% confidence level. For the two simplified dark matter production models considered, the observed (expected) lower limits on the mediator masses are both 950 (1150) GeV for 1 GeV dark matter mass.

Thesis Supervisor: Christoph E.M. Paus
Title: Professor

Acknowledgments

This is the acknowledgements section. You should replace this with your own acknowledgements.

Contents

1	The Standard Model	9
1.1	Strong Interactions	11
1.2	Hadrons	12
1.3	Electroweak Interactions	13
1.4	Electroweak Symmetry Breaking	14
1.5	Fermion Masses	16
1.6	Flavor Mixing	17
1.7	Summary	18
2	Dark Matter	21
2.1	Astrophysical Evidence	22
2.1.1	Galactic Clusters	22
2.1.2	Galactic Rotation Curves	23
2.1.3	Gravitational Lensing	24
2.1.4	Cluster Collisions	25
2.2	Relic Density	28
2.3	Dark Matter Candidates	30
2.3.1	Weakly-Interacting Massive Particles	31
2.3.2	Axions	31
2.3.3	Sterile Neutrinos	32
2.4	Simplified Models for LHC	34
2.5	Non-collider Searches	36
2.5.1	Direct Detection	36

2.5.2	Indirect Detection	39
2.6	Summary	41

Chapter 1

The Standard Model

The Standard Model (SM) of particle physics describes the physical properties and dynamics of fermions, the fundamental constituents of matter, and their interactions in the language of a Lorentz-invariant quantum field theory (QFT). The Standard Model consists of a set of fermion fields, shown in Table 1.1 and the local gauge symmetry group that acts on them

$$G_{\text{SM}} = \text{SU}(3)_C \times \text{SU}(2)_L \times \text{U}(1)_Y, \quad (1.1)$$

which is composed of the subgroups

$$\begin{aligned} G_{\text{QCD}} &= \text{SU}(3)_C && \text{and} \\ G_{\text{EWK}} &= \text{SU}(2)_L \times \text{U}(1)_Y, \end{aligned} \quad (1.2)$$

corresponding to the strong and electroweak interactions, respectively. Each fermion field exists in a unique representation of G_{SM} , also summarized in Table 1.1. The possible representations of $\text{SU}(3)_C$ are triplet, conjugate, and singlet, denoted by **3**, **$\bar{3}$** , and **1**, respectively, while the possible representations of $\text{SU}(2)_L$ are doublet and singlet, denoted by **2** and **1**, respectively. All fermions exist in the singlet representation of $\text{U}(1)_Y$, only distinguished by differing values of the weak hypercharge Y . Conversely, all fermions in non-singlet representations of $\text{SU}(3)_C$ and $\text{SU}(2)_L$ have

the same interaction strength, a feature known as universality.

Table 1.1: The categories of SM fermions and the action of the SM local gauge symmetry group G_{SM} . Each category contains three members, one for each generation of the Standard Model. A corresponding table exists for the charge conjugated fields representing the anti-fermions. The subscripts L and R denote whether the field is left- or right-handed.

Name	Symbol	Y	$\text{SU}(2)_L$ rep.	$\text{SU}(3)_C$ rep.
Left-handed quark	q_L	$1/6$	2	3
Right-handed up-type quark	u_R	$2/3$	1	3
Right-handed down-type quark	d_R	$-1/3$	1	3
Left-handed lepton	ℓ_L	$-1/2$	2	1
Right-handed charged lepton	e_R	-1	1	1
Right-handed neutrino	ν_R	$1/6$	1	1

For each category of fermion listed in Table 1.1, there exist three generations or copies in the Standard Model, identical except for differing masses. The lepton electroweak doublets contain the left-handed charged leptons and neutrinos

$$\ell_L = \begin{pmatrix} \nu_e \\ e_L^- \end{pmatrix}, \begin{pmatrix} \nu_\mu \\ \mu_L^- \end{pmatrix}, \begin{pmatrix} \nu_\tau \\ \tau_L^- \end{pmatrix}, \quad (1.3)$$

and the right-handed lepton singlets contain the right-handed projections of the same leptons and neutrinos. The quark electroweak doublets contain the left-handed up-type and down-type quarks

$$q_L = \begin{pmatrix} u_L \\ d_L \end{pmatrix}, \begin{pmatrix} c_L \\ s_L \end{pmatrix}, \begin{pmatrix} t_L \\ b_L \end{pmatrix}, \quad (1.4)$$

and the right-handed quark singlets contain the right-handed projections of the same quarks. Quarks also exist in a strong triplet, which will be denoted with a superscript c as necessary.

1.1 Strong Interactions

The strong interactions of quarks and gluons are described by quantum chromodynamics (QCD), with the Lagrangian

$$\mathcal{L}_{\text{QCD}} = i\bar{q}_f^a D^\mu{}^{ab} q_f^b + m_f \bar{q}_f^a q_f^a - \frac{1}{4} G_{\mu\nu}^a G^{a,\mu\nu} + \theta \frac{g_s^2}{72\pi^2} \epsilon_{\mu\nu\rho\sigma} G^{c,\mu\nu} G^{c,\rho\sigma}, \quad (1.5)$$

where repeated indices are contracted. The q_f^a are the quark-field Dirac spinors of flavor $f \in \{u, d, c, s, t, b\}$, color $a \in \{r, g, b\}$ (the basis elements of the triplet representation), and mass m_f . The first term in Equation 1.5 contains the QCD covariant derivative

$$D_\mu^{ab} = \delta^{ab} \partial_\mu - ig_s \sum_c t_c^{ab} G_{c,\mu}, \quad (1.6)$$

where g_s is the strong interaction coupling strength, t_c are the eight 3×3 Hermitian traceless matrices that serve as the generators of the triplet representation of $\text{SU}(3)_C$, and G_c are the corresponding eight gluon fields. The third term in Equation 1.5 contains the gluon field strength tensors

$$G_{\mu\nu}^a = \partial_\mu G_\nu^a - \partial_\nu G_\mu^a - g_s f^{abc} G_\mu^b G_\nu^c, \quad (1.7)$$

where f^{abc} are the structure constants of $\text{SU}(3)_C$. The non-Abelian structure of the $\text{SU}(3)_C$ group allows for 3-gluon and 4-gluon interactions in addition to the quark-antiquark-gluon interactions.

The last term in Equation 1.5 violates CP conservation and produces a non-zero electric dipole moment (EDM) for the neutron. Experimental limits on the neutron EDM constrain the observed QCD vacuum angle θ to be smaller than 10^{-10} . The Peccei-Quinn theory provides a possible explanation for this contradiction by introducing the hypothetical axion particle a with the following Lagrangian

$$\mathcal{L}_a = \frac{1}{2} \partial_\mu a \partial^\mu a + \frac{g_s^2}{72\pi^2} \frac{a}{f_a} \epsilon_{\mu\nu\rho\sigma} G^{c,\mu\nu} G^{c,\rho\sigma} \quad (1.8)$$

, where f_a is axion decay constant that determines its characteristic scale. The second

term in Equation 1.8 cancels the last term in Equation 1.5 when the axion field dynamically assumes its vacuum expectation value $\langle a \rangle = -f_a\theta$. The axion is a potential dark matter candidate and will be discussed further in Section 2.3.2.

1.2 Hadrons

Free quarks and gluons are not observed in nature, only in bound states called hadrons. This is a consequence of two factors: color confinement and asymptotic freedom.

Color confinement is the hypothesis that colored objects are always confined to color singlet states and that no objects with non-zero color charge can propagate as free particles. Thus, quarks can only exist in bound states of a quark-antiquark pair or three quarks, called mesons and baryons, respectively. Since gluons carry a color charge, they are confined to hadrons as well. Confinement is a low-energy non-perturbative phenomenon, occurring only below the QCD confinement scale Λ_{QCD} . An analytic proof of color confinement does not exist currently; however, the running of the strong coupling constant $\alpha_s = g_s^2/4\pi$ provides a mechanism for it.

Due to higher-order corrections to propagators in a QFT, physical quantities such as coupling constants and masses acquire a scale-dependence, where the value of the quantity changes as a function of the probed energy scale q^2 . The process of recovering scale-invariance is called renormalization and ensures that any divergent terms from the higher-order corrections cancel out in the physical values. Given the value of an arbitrary coupling constant α at some known scale μ^2 , the value of α at arbitrary scale q^2 is

$$\alpha(q^2) = \frac{\alpha(\mu^2)}{1 - \alpha(\mu^2) [\Pi(q^2) - \Pi(\mu^2)]}, \quad (1.9)$$

where $\Pi(q^2)$ and $\Pi(\mu^2)$ are the self-energy correction of the propagator at scales q^2 and μ^2 . While these individual terms are separately divergent, their difference is finite and calculable.

For values of q^2 and μ^2 larger than the confinement scale Λ_{QCD} , the difference

between the gluon self-energy corrections to one-loop order is given by

$$\Pi_s(q^2) - \Pi_s(\mu^2) \approx -\frac{\beta}{4\pi} \ln \left(\frac{q^2}{\mu^2} \right) \quad (1.10)$$

where β depends on the number of quark and gluon loops. For N_c colors and N_f quark flavors with mass below $|q|$,

$$\beta = \frac{11N_c - 2N_f}{12\pi}. \quad (1.11)$$

In the Standard Model, $N_c = 3$ and $N_f \leq 6$ regardless of energy, thus β is always positive. Combining Equations 1.9 and 1.10, the evolution of α_s is given by

$$\alpha_s(q^2) = \frac{\alpha_s(\mu^2)}{1 + \beta \alpha_s(\mu^2) \ln \left(\frac{q^2}{\mu^2} \right)} \approx \frac{1}{\beta \ln \left(\frac{q^2}{\Lambda_{\text{QCD}}^2} \right)} \quad (1.12)$$

for a sufficiently large energy scale $q^2 \gg \Lambda_{\text{QCD}}^2$. Through electron-positron collisions, the value of α_s at the Z -pole has been measured to be $\alpha_s(m_Z^2) = 0.1181 \pm 0.0011$ with a corresponding confinement scale of $\Lambda_{\text{QCD}} = 218$ MeV.

From Equation 1.12, we see that α_s decreases with increasing q^2 . At $|q| \sim 1$ GeV, the value of α_s is of $\mathcal{O}(1)$ confining quarks and gluons to hadrons in a strongly-bound non-perturbative state. However, $|q| \gtrsim 100$ GeV, we have $\alpha_s \approx 0.1$ which is small enough that perturbation theory can be used and quarks can be treated as quasi-free particles. This property of QCD is known as asymptotic freedom.

1.3 Electroweak Interactions

The electroweak interactions of fermions are described by $SU(2)_L \times U(1)_Y$ gauge group, with the Lagrangian

$$\mathcal{L}_{\text{EWK}} = i\bar{\psi}_i \not{D} \psi_i - \frac{1}{4} \vec{W}_{\mu\nu} \cdot \vec{W}^{\mu\nu} - \frac{1}{4} B_{\mu\nu} B^{\mu\nu} \quad (1.13)$$

where repeated indices are contracted and $\psi \supseteq \{q_L, u_R, d_R, \ell_L, e_R, \nu_R\}$ is the set of SM fermions, and the gauge field tensors are given by

$$\begin{aligned} B_{\mu\nu} &= \partial_\mu B_\nu - \partial_\nu B_\mu \quad \text{and} \\ \vec{W}_{\mu\nu} &= \partial_\mu \vec{W}_\nu - \partial_\nu \vec{W}_\mu + g \vec{W}^\mu \times \vec{W}^\nu, \end{aligned} \quad (1.14)$$

where \vec{W}_μ and B_μ are the gauge fields for $SU(2)_L$ and $U(1)_Y$, respectively, and g is the coupling strength for $SU(2)_L$. The first term in Equation 1.13 contains the EWK covariant derivative

$$D_\mu = \partial_\mu - ig \vec{T} \cdot \vec{W}_\mu - ig' Y B_\mu, \quad (1.15)$$

where g' is the coupling strength for $U(1)_Y$, Y is the $U(1)_Y$ hypercharge of the fermion field, and \vec{T} are the generators of the doublet representation of $SU(2)_L$. The generators can be written in terms of the Pauli spin matrices $\vec{T} = \vec{\sigma}/2$ and only have non-zero action on left-handed particles. The values of the hypercharge Y shown in Table 1.1 are chosen such that the physical electric charge of each fermion is given by $Q = T_3 + Y$.

Notice that Equation 1.13 does not contain a Dirac mass term like that found in Equation 1.5. This is because the term

$$m \bar{\psi} \psi = m (\bar{\psi}_L \psi_R + \bar{\psi}_R \psi_L) \quad (1.16)$$

mixes the left-handed and right-handed fermions leading to a Lagrangian that is no longer invariant under $SU(2)_L$. As the observed fermions are not massless, the Lagrangian given in Equation 1.13 is incomplete and an additional mechanism needs to be introduced to produce non-zero fermion masses.

1.4 Electroweak Symmetry Breaking

Spontaneous electroweak symmetry breaking provides the mechanism we need, as well as providing masses to the weak gauge bosons. The $SU(2)_L$ symmetry is broken by introducing a left-handed complex scalar doublet ϕ with $Y_\phi = 1/2$ to the Lagrangian

in the following manner

$$\mathcal{L}_{\text{EWK}} \mapsto \mathcal{L}_{\text{EWK}} + |D_\mu \phi|^2 + \mu^2 \phi^2 - \lambda |\phi|^4. \quad (1.17)$$

We choose to write this complex doublet, known as the complex Higgs field, in terms of four real-valued fields so that

$$\phi = \frac{1}{\sqrt{2}} \begin{pmatrix} \phi_1 + i\phi_2 \\ \phi_3 + i\phi_4 \end{pmatrix}. \quad (1.18)$$

Fortunately, the two self-interaction terms create a Higgs potential with a degenerate global minimum at the vacuum expectation value (vev)

$$v \equiv \langle |\phi| \rangle = \sqrt{\frac{\mu^2}{\lambda}}, \quad (1.19)$$

and through gauge rotations we set $\langle \phi_{1,2,4} \rangle = 0$, removing three degrees of freedom and producing three massless Nambu-Goldstone bosons. The remaining degree of freedom is the real Higgs field H which expresses small perturbations around the vev in the third component of the complex Higgs field $\phi_3 = v + H$.

The kinetic term in Equation 1.17 couples the complex Higgs field to the EWK gauge bosons as follows at the vev

$$|D_\mu \phi|^2 = \frac{v^2}{8} \left[(gW_\mu^1)^2 + (gW_\mu^2)^2 + (g'B_\mu - gW_\mu^3)^2 \right]. \quad (1.20)$$

Diagonalizing this term gives rise to the three massive weak bosons and the massless photon that we observe in nature:

$$\left. \begin{aligned} W_\mu^\pm &\equiv \frac{1}{\sqrt{2}} (W_\mu^1 \mp W_\mu^2) \\ Z_\mu &\equiv \cos \theta_W W_\mu^3 - \sin \theta_W B_\mu \\ A_\mu &\equiv \sin \theta_W W_\mu^3 + \cos \theta_W B_\mu \end{aligned} \right| \begin{aligned} m_W &= \frac{1}{2} v g \\ m_Z &= \frac{1}{2} v \sqrt{g^2 + (g')^2} \\ m_A &= 0, \end{aligned} \quad (1.21)$$

where $\tan \theta_W = g'/g$. With this, we rewrite Equation 1.13 in terms of the observed

electromagnetic, charged weak, and neutral weak currents as follows:

$$\begin{aligned}\mathcal{L}_{\text{EWK}} = & \bar{\psi}_i (i\cancel{d} - eQ\cancel{A}) \psi_i - \frac{g}{2\sqrt{2}} \bar{\psi}_i \left(T^+ W^+ + T^- W^- \right) \psi_i - \frac{1}{2} m_W^2 W_\mu^+ W^{-\mu} \\ & - \frac{g}{2 \cos \theta_W} \bar{\psi}_i (g_V - g_A \gamma^5) \cancel{Z} \psi_i - \frac{1}{2} m_Z^2 Z_\mu Z^\mu,\end{aligned}\quad (1.22)$$

where $e = g' \cos \theta_W$ is the charge of the electron, $T^\pm = (T_1 \mp iT_2)/\sqrt{2}$ are the weak isospin raising and lowering operators, and $g_V = T_3$ and $g_A = T_3 - 2Q \sin^2 \theta_W$ are the vector and axial-vector couplings for the neutral weak current.

We can also expand Equation 1.17 about the vev giving us the following Higgs Lagrangian

$$\begin{aligned}\mathcal{L}_H = & \frac{1}{2} \partial_\mu H \partial^\mu H - \frac{1}{2} m_H^2 H^2 + \frac{m_H^2}{2v} H^3 + \frac{2m_W^2}{v} W_\mu^+ W^{-\mu} H + \frac{m_Z^2}{v} Z_\mu Z^\mu H \\ & + \frac{m_H^2}{8v^2} H^4 + \frac{m_W^2}{v^2} W_\mu^+ W^{-\mu} H^2 + \frac{m_Z^2}{2v^2} Z_\mu Z^\mu H^2,\end{aligned}\quad (1.23)$$

where $m_H = \mu\sqrt{2}$. Thus, we see that the real Higgs field H has trilinear and quartic couplings to itself and the weak gauge bosons with coupling strengths proportional to the mass squared of the appropriate boson. This suggests a way to introduce fermion masses through the Higgs field.

1.5 Fermion Masses

Introducing Yukawa couplings between the complex Higgs field ϕ and the SM fermion fields enables us to add mass terms for the fermions. First, we start with the terms for charged leptons,

$$\mathcal{L}_Y^{\text{leptons}} = -\bar{\ell}_L Y_e \phi e_R - \bar{e}_R Y_e^\dagger \phi^\dagger \ell_L,\quad (1.24)$$

where Y_e is the Yukawa matrix for the charged leptons. In general, Yukawa matrices and thus mass matrices are non-diagonal and hence we need to convert from the electroweak eigenstates $f_{L,R}$ to the mass eigenstates $\tilde{f}_{L,R} = U_{L,R}^f f_{L,R}$ where $U_{L,R}^f$ is a

unitary matrix. With this we rewrite Equation 1.24 in terms of the mass eigenstates

$$\begin{aligned}\mathcal{L}_Y^{\text{leptons}} &= -\bar{\tilde{\ell}}_L U_L^e Y_e \phi U_R^{e\dagger} \tilde{e}_R - \bar{\tilde{e}}_R U_R^e Y_e^\dagger \phi^\dagger U_L^{e\dagger} \tilde{\ell}_L \\ &= -\bar{\tilde{\ell}}_L \tilde{Y}_e \phi \tilde{e}_R - \bar{\tilde{e}}_R \tilde{Y}_e^\dagger \phi^\dagger \tilde{\ell}_L,\end{aligned}\quad (1.25)$$

where $\tilde{Y}_e = U_L^e Y_e U_R^{e\dagger}$ is the diagonalized Yukawa matrix for the charged leptons. After electroweak symmetry breaking, these terms become

$$\begin{aligned}\mathcal{L}_Y^{\text{leptons}} &= -\frac{v+H}{\sqrt{2}} \left(\bar{\tilde{e}}_L \tilde{Y}_e \tilde{e}_R + \bar{\tilde{e}}_R \tilde{Y}_e^\dagger \tilde{e}_L \right) \\ &= -\left(1 + \frac{H}{v} \right) \left(\bar{\tilde{e}}_L \tilde{M}_e \tilde{e}_R + \bar{\tilde{e}}_R \tilde{M}_e^\dagger \tilde{e}_L \right) \\ &= -\tilde{M}_e \bar{e} e - \frac{\tilde{M}_e}{v} \bar{e} e H,\end{aligned}\quad (1.26)$$

where $\tilde{M}_e = v \tilde{Y}_e / \sqrt{2}$ is the diagonalized mass matrix for the charged leptons and e is the set of massive Dirac spinors for the charged leptons.

From Equation 1.26, we see that the Yukawa couplings between the complex Higgs field ϕ and the charged leptons result in a Dirac mass term and a coupling to the real Higgs field H that is proportional to the mass of the charged leptons and the vev. The same procedure is used to introduce mass terms for the down-type quarks whereas for the neutrinos and up-type quarks we must use the conjugate doublet $\phi_c = -i\sigma_2\phi^*$ in place of ϕ to obtain the same result.

1.6 Flavor Mixing

For the charged leptons and up-type quarks, it is possible to define a basis of simultaneous electroweak and mass eigenstates, so in practice $\tilde{Y}_{e,u} = Y_{e,u}$ as $U_L^{e,u} = U_R^{e,u} = \mathbf{I}$. However, it is not possible to do this for the neutrinos at the same time as the charged leptons or for the down-type quarks at the same time as the up-type quarks.

In Equation 1.22, the charged current term involves interactions between the up-type and down-type quarks and is not preserved under the transform $f \rightarrow \tilde{f}$. Writing

this in terms of the mass eigenstates we have

$$\begin{aligned}\mathcal{L}_{\text{CC}} &= -\frac{g}{2\sqrt{2}} \left(\bar{u}_L T^+ W^+ d_L + \bar{d}_L T^- W^- u_L \right) \\ &= -\frac{g}{2\sqrt{2}} \left(\bar{u}_L T^+ W^+ V_{\text{CKM}} \tilde{d}_L + \bar{\tilde{d}}_L T^- W^- V_{\text{CKM}}^\dagger u_L \right),\end{aligned}\quad (1.27)$$

where $V_{\text{CKM}} = U_L^{u\dagger} U_L^d$ is the Cabibbo-Kaboyshi-Maskawa matrix and $u_L = \tilde{u}_L$ by construction. The CKM matrix is unitary with four free parameters, the mixing angles between quark generations $\phi_{12} = 13.1$, ϕ_{23} , and ϕ_{13} as well as a CP-violating phase δ . In terms of these parameters, the CKM matrix is

$$V_{\text{CKM}} = \begin{pmatrix} c_{12} & s_{12} & 0 \\ -s_{12} & c_{12} & 0 \\ 0 & 0 & 1 \end{pmatrix} \times \begin{pmatrix} 1 & 0 & 0 \\ 0 & c_{23} & s_{23} \\ 0 & -s_{23} & c_{23} \end{pmatrix} \times \begin{pmatrix} c_{13} & 0 & s_{13} e^{-i\delta} \\ 0 & 1 & 0 \\ -s_{13} e^{i\delta} & 0 & c_{13} \end{pmatrix}, \quad (1.28)$$

where $s_{ij} = \sin \phi_{ij}$ and $c_{ij} = \cos \phi_{ij}$. It has been experimentally determined that the CKM is mostly diagonal with $s_{13} \ll s_{23} \ll s_{12} \ll 1$.

The equivalent mixing matrix for the neutrinos is the Pontecorvo-Maki-Nakagawa-Sakata matrix U_{PMNS} , which converts from the mass eigenstates ν_1 , ν_2 , and ν_3 to the electroweak eigenstates ν_e , ν_μ , ν_τ . Unlike the CKM matrix, the PMNS is non-diagonal resulting in stronger mixing in the neutrino sector. The values of the mixing angles θ_{12} , θ_{23} , and θ_{13} have been measured in neutrino oscillation experiments while the CP-violating phase δ' has not yet been directly measured. From cosmological measurements, it is known that the sum of the neutrino masses is less than one eV.

1.7 Summary

The Standard Model has a total of 26 free parameters and 17 physical particles. The parameters are the twelve Yukawa couplings for the fermions, the four parameters of the CKM matrix, the four parameters of the PMNS matrix, the three coupling constants g_s , g , and g' , the Higgs vacuum expectation value v , the Higgs mass m_H , and the QCD vacuum angle θ . The best fit values of the SM parameters, excluding

Table 1.2: The free parameters of the Standard Model, not including masses.

Parameter	Description	Best Fit Value
ϕ_{12}	CKM 12-mixing angle	13.1°
ϕ_{23}	CKM 23-mixing angle	2.4°
ϕ_{13}	CKM 13-mixing angle	0.4°
δ	CKM CP-violating phase	0.995
$\sin^2 \theta_{12}$	PMNS 12-mixing angle	0.297
$\sin^2 \theta_{23}$	PMNS 23-mixing angle	0.437
$\sin^2 \theta_{13}$	PMNS 13-mixing angle	0.0214
δ'	PMNS CP-violating phase	1.35
g_s	SU(3) _C coupling constant	1.221
g	SU(2) _L coupling constant	0.652
g'	U(1) _Y coupling constant	0.357
v	Higgs vacuum expectation value	246 GeV
θ	QCD vacuum angle	$< 10^{-10}$

masses, are summarized in Table 1.2.

The physical particles are the single-particle states of the various mass eigenfields and their properties are summarized in Table 1.3. Each of the fermion fields has a corresponding anti-particle with the electromagnetic and color charges inverted. Most of these single-particle states have finite lifetimes and decay to lower energy configurations. The only particles whose decays have not been observed are the photon, the electron, the neutrinos, and the proton (a baryon of flavor content uud). Additionally, stable bound states of protons and neutrons (a baryon of flavor content udd) exist in the form of atomic nuclei.

Table 1.3: The physical particles of the Standard Model.

Name	Symbol	Spin	Charge	Mass
up quark	u	$\frac{1}{2}$	$\frac{2}{3}$	2.2 MeV
down quark	d	$\frac{1}{2}$	$-\frac{1}{3}$	4.7 MeV
charm quark	c	$\frac{1}{2}$	$\frac{2}{3}$	1.28 GeV
strange quark	s	$\frac{1}{2}$	$-\frac{1}{3}$	95 MeV
top quark	t	$\frac{1}{2}$	$\frac{2}{3}$	173 GeV
bottom quark	b	$\frac{1}{2}$	$-\frac{1}{3}$	4.18 GeV
electron neutrino	ν_e	$\frac{1}{2}$	0	-
electron	e	$\frac{1}{2}$	-1	511 keV
muon neutrino	ν_μ	$\frac{1}{2}$	0	-
muon	μ	$\frac{1}{2}$	-1	105 MeV
tau neutrino	ν_τ	$\frac{1}{2}$	0	-
tau	τ	$\frac{1}{2}$	-1	1.78 GeV
gluon	g	1	0	0
photon	γ	1	0	0
Z boson	Z	1	0	91.2 GeV
W boson	W^\pm	1	± 1	80.4 GeV
Higgs boson	H	0	0	125 GeV

Chapter 2

Dark Matter

As a theory of the fundamental particles and forces of nature, the Standard Model should also help explain physics at the largest scales. The Λ CDM model best explains all current cosmological observations including the structure of the cosmic microwave background; the abundances of hydrogen, helium, and lithium; the large-scale structure in the distribution of galaxies, and the accelerating expansion of the universe. However, the latest results from the Planck collaboration show that baryonic matter (matter consisting of various combinations of protons, neutrons, and electrons) only contributes $\sim 5\%$ of the total energy of the universe, with radiation (photons and relativistic neutrinos) contributing less than a hundredth of a percent.

The remaining 95% of energy comes from just two sources: $\sim 27\%$ from non-relativistic non-baryonic matter referred to as dark matter and $\sim 68\%$ from an unknown form of energy that permeates all of space referred to as dark energy. Current observations show that dark energy is uniform in space and time producing a similar effect to that of the cosmological constant in the Einstein field equations of general relativity. Not much else is known about dark energy, although there are many experiments attempting to discover additional properties. The work in this thesis shall focus on trying to explain dark matter.

Dark matter cannot be explained by the 17 particles of the Standard Model (see Section 2.3), yet its gravitational effects have been observed in many circumstances. The rest of this chapter will cover the astrophysical evidence for dark matter (Sec-

tions 2.1 and 2.2), various dark matter candidates (Section 2.3) and the models investigated at the LHC (Section 2.4), and non-collider searches for dark matter (Section 2.5).

2.1 Astrophysical Evidence

All existing evidence for dark matter comes from astrophysical observations of its gravitational effects on the universe at various length scales. We shall focus on four different sources of evidence: the average velocity of galaxies in clusters, the rotation curves of spiral galaxies, strong gravitational lensing, and merging galactic clusters. The evidence presented here is not exhaustive, see Reference ?? for more detail.

2.1.1 Galactic Clusters

Galactic clusters are the largest gravitational bound systems, with the orbital velocities of the individual clusters determined by the total gravitational mass of the cluster. Applying the Virial Theorem gives the explicit relation

$$v^2 = \frac{GM}{2r}, \quad (2.1)$$

where v is the average orbital velocity of a galaxy in the cluster, r is the average separation between galaxies in the cluster, M is the total gravitational mass of the cluster, and G is the Newtonian constant of gravitation. In 1933, Fritz Zwicky measured the average orbital velocity of the Coma cluster and discovered that it was a factor of ten larger than the observed visible mass of the Coma cluster, leading to the conclusion that the majority of the cluster consisted of non-luminous matter. Today studies show that stars only contribute 1% of the total cluster mass, with a hot, baryonic intracluster medium and dark matter contributing the remaining 14% and 85% of the total cluster mass, respectively.

2.1.2 Galactic Rotation Curves

Spiral galaxies are stable gravitational bound systems with stars and interstellar gas rotating around the galactic center in nearly circular orbits in a single plane. For these galaxies, the orbit of an individual star is stable when the gravitational force acting on the star balances the centripetal acceleration of the star. With this condition, the expected stellar velocity v is a function of distance r from the galactic center given by

$$v = \sqrt{\frac{GM(r)}{r}} \quad (2.2)$$

where $M(r)$ is the total gravitational mass inside radius r . Thus, past a certain critical radius r_c , the stellar velocity should fall with as $r^{1/2}$ as the mass of the galaxy is no longer increasing.

In 1980, Vera Rubin and Kent Ford observed that instead of decreasing at distances outside the visible galaxy, the stellar velocity stayed constant out to a very great distance, necessitating an additional non-luminous source of mass. The most common explanation for this missing mass is the existence of an isotropic dark matter halo surrounding the galaxy. With the inclusion of interstellar gas, the total mass inside radius r is given by

$$M(r) = 4\pi \int_0^r dr' (r')^2 [\rho_S(r') + \rho_g(r') + \rho_{DM}(r')], \quad (2.3)$$

where ρ_S , ρ_g , and ρ_{DM} are the density profiles of the stars, interstellar gas, and dark matter in the galaxy, respectively. Once these densities have been specified, it is possible to plot the fraction of the total stellar velocity due to each mass source as a function of distance from the galactic center.

Figure 2-1 shows the results of doing this using the observed stellar and interstellar mass density profiles and the expected density from an isotropic dark matter halo for two different spiral galaxies. In both cases, this reproduces the observed flat galactic rotation curve incredibly well, lending strong support for the existence of galactic dark matter halos.

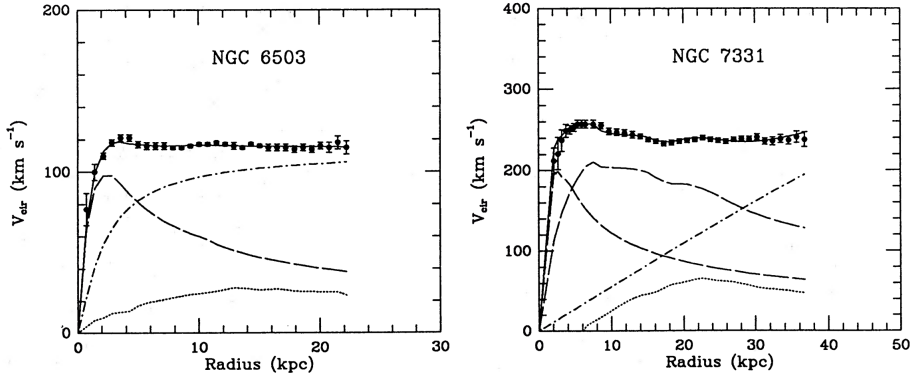


Figure 2-1: The observed (points) and fitted (solid line) rotation curves for two sample galaxies. The fit consists of three components: the stellar component (dashed), the interstellar gas (dotted), and the dark matter halo (dash-dotted). Reprinted from Reference [1].

2.1.3 Gravitational Lensing

As a consequence of Einstein's equivalence principle, a massive body will deflect light, a phenomenon known as gravitational lensing. In the language of general relativity, this means that the photons take the path given by the geodesic lines following the curvature of space-time due to the massive body. For most observations of gravitational lensing due to astrophysical bodies, the physical size of the lensing object is much smaller than the distance between observer, lens, and source allowing us to use the thin lens approximation. Approximating the lens as a planar distribution of matter, the angular deflection is given by

$$\vec{\alpha}(\vec{x}) = \frac{4G}{c^2} \int d^2x' \frac{\vec{x} - \vec{x}'}{|\vec{x} - \vec{x}'|^2} \int dz \rho(\vec{x}', z) \quad (2.4)$$

where \vec{x} is a two-dimensional vector in the plane of the lens, z is the perpendicular distance from the plane of the lens, and ρ is the three dimensional density. If the source is treated as a point mass, this reduces to

$$\alpha = \frac{4G}{c^2} \cdot \frac{M}{b} \quad (2.5)$$

where $b = |\vec{x} - \vec{x}'|$ is the impact parameter and M is the total mass of the object. Thus, measuring the angle of deflection due to gravitational lensing around an astrophysical object provides an independent measurement of the total mass of the body which can be compared against the mass of the luminous objects in the body.

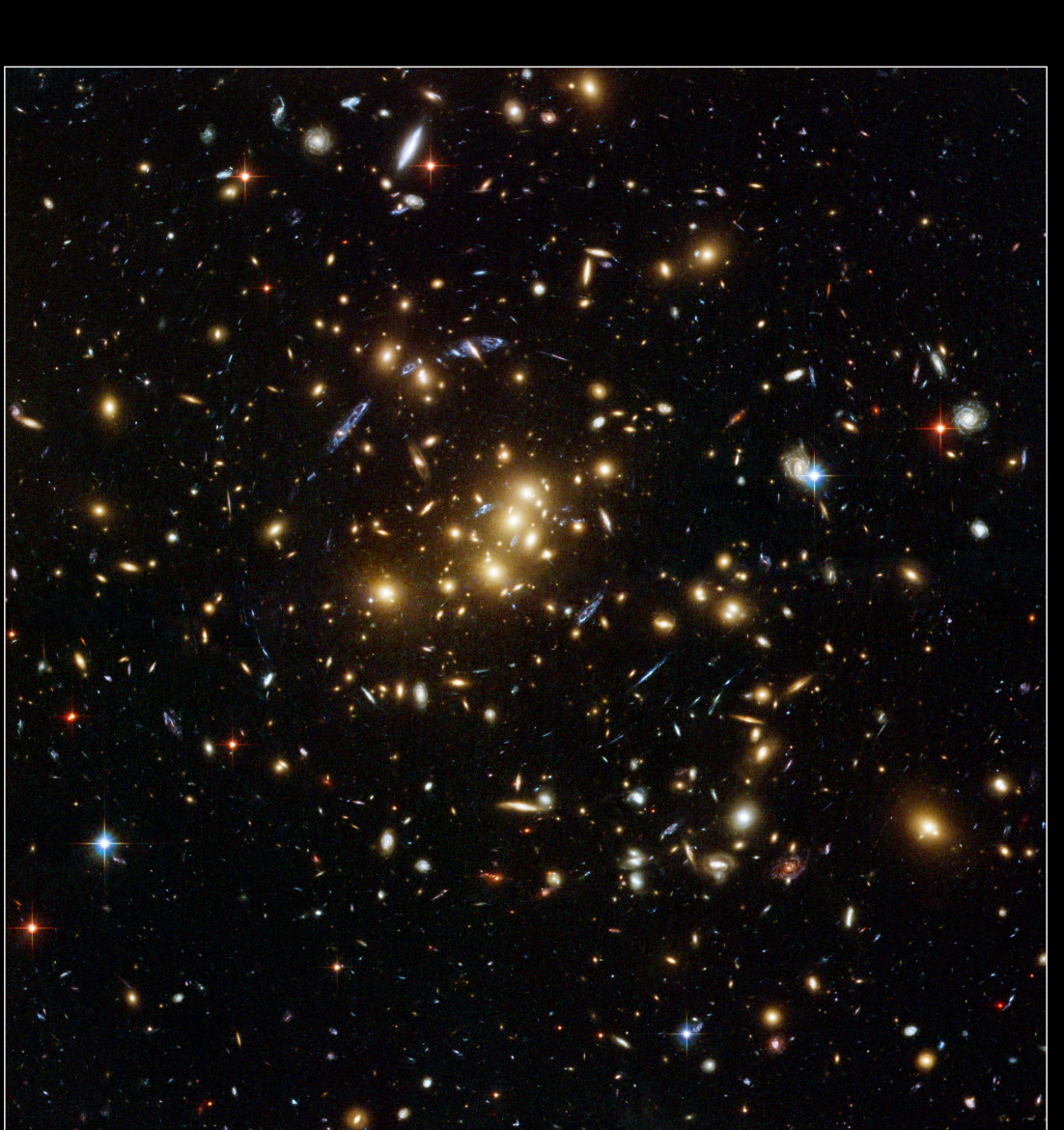
Depending on the mass of the deflecting body and impact parameter, the size of deflection can fall into three different regimes. The first of these is called strong lensing where the curving of space-time is so strong that light can travel multiple paths around the lens and still reach the observer. If the source is directly behind a circular lens, light travels around all sides of the lens and appears as an Einstein ring, while if the source is offset or the lens is non-circular, the source will instead appear in multiple locations as if viewed from slightly different angles. An example of strong lensing is shown in Figure 2-2.

The next regime is known as weak lensing, where the deflection is enough to distort the image of the source but not enough to result in multiple images. The shear of this distortion can be converted into a map of the projected mass distribution. True weak lensing results in circular “*E*-mode” patterns while sources of systematic uncertainty produce both “*E*-mode” and curl-like “*B*-mode” patterns. Thus, requiring a zero “*B*-mode” contribution assures that the measured mass distribution is accurate. Figure 2-3 shows the observed shear of half a million galaxies measured in the Hubble Space Telescope COSMOS survey.

The final regime is the microlensing that occurs when a lens moves relative to a luminous source. As the lens passes in front of the source, it will temporarily increase the apparent luminosity of the source, enabling a mass measurement of the lens. Microlensing results show that rocky exoplanets orbit other stars and that these planets cannot form the bulk of dark matter in the Milky Way.

2.1.4 Cluster Collisions

Additionally, gravitational lensing measurements of galactic cluster collisions provide support for dark matter and help constrain its properties. Figure 2-4 shows the merging cluster 1E0657-558. By comparing the weak lensing reconstruction of



Galaxy Cluster Cl 0024+17 (ZwCl 0024+1652)
Hubble Space Telescope • ACS/WFC

NASA, ESA, and M.J. Jee (Johns Hopkins University)

STScI-PRC07-17b

Figure 2-2: Strong gravitational lensing around galaxy cluster CL0024+17, consisting of the gravitationally bound yellow, elliptical galaxies. The elongated blue objects are from much more distant galaxies behind the cluster which are distorted into arcs due to gravitational lensing from the dark matter halo surrounding the cluster. Figure credit: NASA, ESA, M.J. Jee and H. Ford (Johns Hopkins University)

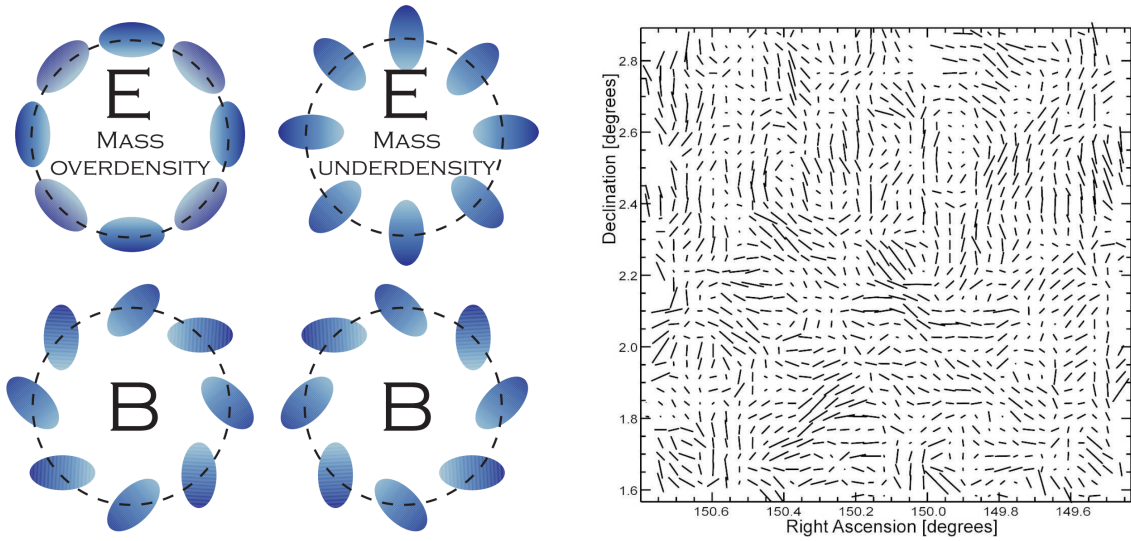


Figure 2-3: Left: Examples of circular “E-mode” and curl-like “B-mode” patterns. Right: The observed ellipticities of half a million distant galaxies within the 2 square degree Hubble Space Telescope COSMOS survey. Reprinted fom Reference [1].

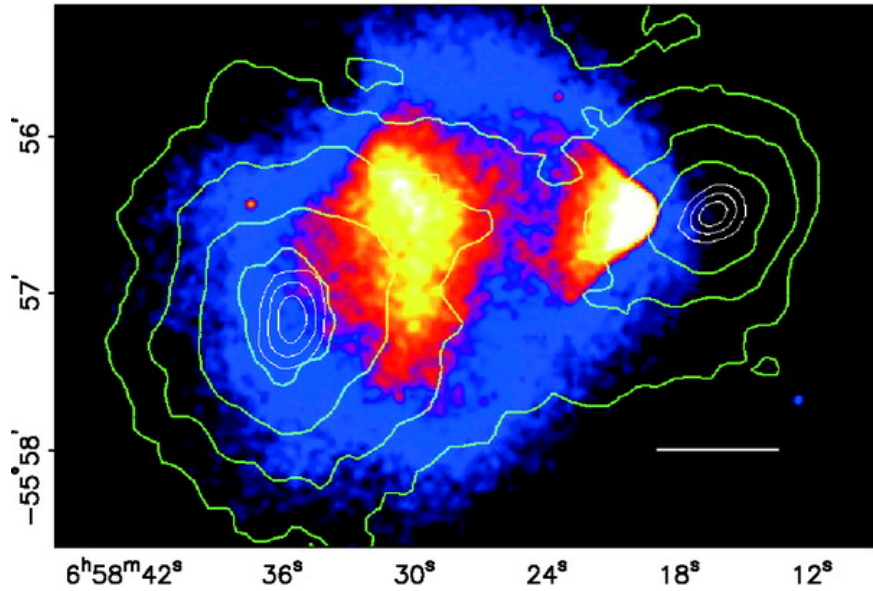


Figure 2-4: The merging cluster 1E0657-558. The green contours show the weak lensing reconstruction of the gravitational potential of the cluster. The colors indicate the X-ray temperature of the plasma, changing from blue to white as the plasma goes from coolest to hottest. The smaller “bullet” cluster on the right which traversed through the larger cluster on the left. Reprinted from Reference [1].

the gravitational potential of the cluster shown in green contours against temperature color gradient of the X-ray emitting interstellar plasma, it was learned that the gravitational potential of the cluster does not track the dominant baryonic mass contribution coming from the plasma. Instead, the gravitational potential tracks the smaller stellar baryonic mass component. Dark matter must be the dominant gravitational source in the cluster since the center of total mass is offset from the center of baryonic mass. Furthermore, the observation of two gravitational mass centers places strong constraints on the self-interaction of dark matter requiring that the observed mass must have a self-interaction collisional cross section $\sigma/m < 1.25 \text{ cm}^2\text{g}^{-1}$ at a 68% confidence level.

2.2 Relic Density

During the early universe, dark matter (DM) was in thermal equilibrium with the rest of the SM particles with a number density n_χ given by

$$n_\chi^{\text{eq}} = \frac{g}{(2\pi)^3} \int f(\vec{p}) d^3\vec{p}, \quad (2.6)$$

where g is the number of internal degrees of freedom of the DM particle χ and $f(\vec{p})$ is either the Fermi-Dirac or Bose-Einstein distribution, depending on the quantum statistics of the DM particle. At very high temperatures relative to the mass m_χ of the DM particle, dark matter and SM particles rapidly convert back and forth with a DM annihilation rate $\Gamma = \langle \sigma_A v \rangle \cdot n_\chi$, where $\langle \sigma_A v \rangle$ is the thermally averaged product of the total cross section for annihilation σ_A and the relative velocity v of the dark matter particles. After the temperature drops below m_χ , the DM annihilation rate Γ drops below the Hubble expansion rate H of the universe and the DM particles stop annihilating and freeze-out of equilibrium with the SM particles, leaving the DM relic density that we observe today. During the freeze-out process, the time dependence

of the number density n_χ is described by the Boltzmann equation as follows

$$\frac{dn_\chi}{dt} + 3Hn_\chi = -\langle\sigma_A v\rangle [(n_\chi)^2 - (n_\chi^{\text{eq}})^2]. \quad (2.7)$$

The LHS term accounts for the reduction in density due to the expansion of the universe. The two RHS terms account for the change in density due to annihilation and product of DM particles to and from SM particles, respectively.

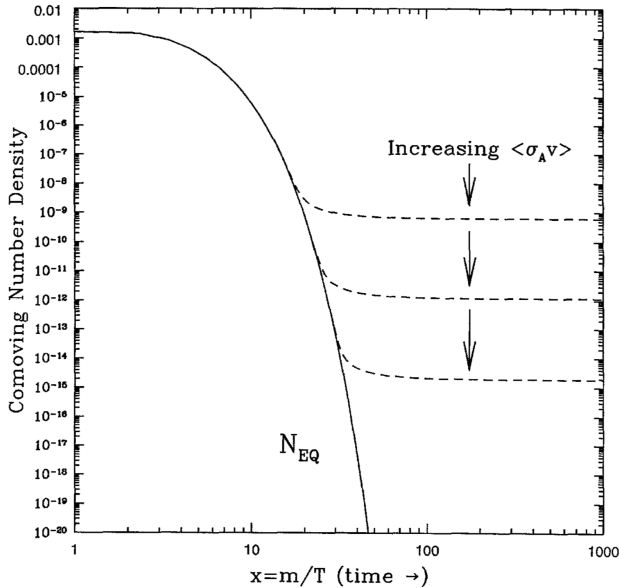


Figure 2-5: Number density of dark matter in the early universe as a function of time. The solid curves are the equilibrium abundance while the dashed curves are the actual abundance after freeze-out. Reprinted from Reference [1].

Figure 2-5 shows the calculated DM number density n_χ as a function of time in the early universe. As the annihilation cross section increases, the relic density decreases as the dark matter particles stay in equilibrium longer. We shall make an order-of-magnitude estimate of the relic density by assuming that $\langle\sigma_A v\rangle$ is independent of energy. Freeze-out occurs at the temperature T_f where the expansion rate $H(T)$ equals the annihilation rate $\Gamma(T)$. The temperature dependence of Γ is simply that of n_χ , e.g. $\Gamma \propto T^3$. Meanwhile, the early universe is radiation dominated, so we have that $H \propto T^2$. Furthermore, astrophysical measurements (see Section 2.1) can't give direct bounds on the number density, only on the mass density $\rho_\chi = m_\chi n_\chi$.

Additionally, mass densities are usually expressed as a fraction of the critical density of the universe $\rho_c = 3H^2/(8\pi G)$. Combining all of this, the relic density of dark matter is given by

$$\Omega_\chi \cdot h^2 = \frac{m_\chi n_\chi}{\rho_c} \simeq \frac{10^{-27} \text{ cm}^3 \text{ s}^{-1}}{\langle \sigma_A v \rangle}, \quad (2.8)$$

where $h = H_0/(100 \text{ km s}^{-1} \text{ Mpc}^{-1})$ is the reduced Hubble constant. Thus, to first order the DM relic density depends only on two things: the total DM annihilation cross section σ_A and the mass m_χ of the DM candidate, as after freeze-out $T \ll m_\chi$ and the velocity v is strictly proportional to m_χ . The latest Planck results measure that $\Omega_\chi \cdot h^2 = 0.1200 \pm 0.0012$, providing strong constraints on the possible values of σ_A and m_χ .

2.3 Dark Matter Candidates

Any dark matter candidate must satisfy the following criteria:

- No or extremely weak interactions with photons, e.g. be **dark**
- Weak baryonic interactions to preserve the DM halos discussed in Section 2.1.2
- Weak self-interactions as discussed in Section 2.1.4
- The observed relic density discussed in Section 2.2.

These four criteria place stringent requirements on dark matter candidates. The light neutrinos, the only SM particles satisfying the first three conditions, are excluded as the total neutrino relic density has a bound of $\Omega_\nu \cdot h^2 \leq 0.00067$ at 95% confidence level from analysis of the CMB anisotropies. Big Bang Nucleosynthesis and gravitational microlensing have mostly exclude non-luminous baryonic matter from forming the bulk of dark matter. Thus, most theories of dark matter propose a new fundamental particle as a dark matter candidate. The following sections discuss the most common dark matter candidates, namely weakly-interacting massive particles (WIMPs), axions, and sterile neutrinos.

2.3.1 Weakly-Interacting Massive Particles

The annihilation cross-section of new particle χ with electroweak scale interactions is approximately

$$\langle \sigma_A v \rangle \approx \left(\frac{\alpha \cdot g_\chi^2}{m_\chi} \right)^2 = \left(\frac{e^2}{4\pi} \cdot \frac{(0.8)^2}{100 \text{ GeV}} \right)^2 \simeq 10^{-26} \text{ cm}^3 \text{ s}^{-1}, \quad (2.9)$$

where $\alpha = e^2/4\pi$ is the fine-structure constant, $m_\chi = 100 \text{ GeV}$ is the mass of the particle, and $g_\chi \approx 0.8$ is the effective coupling for the four-point interaction $\chi\bar{\chi} \rightarrow f\bar{f}$. Plugging this into Equation 2.8, we obtain $\Omega_\chi \cdot h^2 \sim 0.1$, which is very close to the observed value. This numerical coincidence motivates a new weakly-interacting massive particle (WIMP) as a good DM candidate.

The only criteria to be a WIMP beyond the generic definition of dark matter is that the mass and interaction strength of the new particle must be approximately that of the EWK scale. Thus, a great many new physics models have WIMPs natively, such as the neutralino in supersymmetry and the lightest Kaluza-Klein particle in theories of universal extra dimensions. In this thesis, we shall focus on a set of simplified models that describe WIMP interactions in a relatively model-independent manner. For more details, see Section 2.4.

2.3.2 Axions

The hypothetical axion particle introduced in Section 1.1 is a dark matter candidate if the axion decay constant f_a is large enough as all axion-SM couplings are inversely proportional to it. Constraints from the observed duration of the neutrino burst from supernova SN 1987A require that $f_a \gtrsim 10^9 \text{ GeV}$, sufficiently high that the axion lifetime exceeds the age of the universe by many orders of magnitude. Thus, the axion is a viable DM candidate due to its long lifetime and weak couplings to SM particles.

After accounting for kinematic mixing with the π^0 and η mesons, the axion mass is given by

$$m_a = \left(\frac{\sqrt{m_u m_d}}{m_u + m_d} \right) \left(\frac{f_\pi}{f_a} \right) m_\pi \simeq \left(\frac{10^7 \text{ GeV}}{f_a} \right) \text{ eV}, \quad (2.10)$$

where f_π is the pion decay constant and m_u , m_d , and m_π are the masses of the up quark, the down quark, and the neutral pion, respectively. From this, we see that the axion mass is inversely proportional to f_a , leading to an upper limit of $m_a \lesssim 10 \text{ meV}$. The Planck measurements of the cosmic microwave background also provide a lower (upper) bound on the axion mass $m_a \gtrsim 10 \mu\text{eV}$ (axion decay constant $f_a \lesssim 10^{12} \text{ GeV}$), otherwise the axion abundance is too high.

The axion obtains a two-photon vertex through loops involving virtual quarks and gluons of the form

$$\mathcal{L}_{a\gamma\gamma} = \frac{1}{4} g_{a\gamma\gamma} \epsilon_{\mu\nu\rho\sigma} F^{\mu\nu} F^{\rho\sigma} a = -g_{a\gamma\gamma} (\vec{E} \cdot \vec{B}) a, \quad (2.11)$$

where $F^{\mu\nu}$ is the electromagnetic field-strength tensor, \vec{E} and \vec{B} are the electric and magnetic fields, respectively, and the coupling constant is

$$g_{a\gamma\gamma} = -\frac{\alpha}{3\pi f_a} \left(\frac{m_u + 4m_d}{m_u + m_d} \right). \quad (2.12)$$

From this, we can see that the axion's coupling to the photon is incredibly small unless in the presence of a strong electromagnetic field. Thus, astrophysical axions are **dark** unless they enter a region with such a field. Searches for axions such as CAST[] and ADMX[] exploit this to try to observe axion-to-photon conversions.

2.3.3 Sterile Neutrinos

In Section 1.5, we introduced mass for the SM fermions through the Higgs mechanism in order to preserve $SU(2)_L$ gauge invariance. However, since the right-handed neutrinos are singlets under the full $SU(3)_C \times SU(2)_L \times U(1)_Y$ gauge of the SM, it is possible to add explicit Majorana mass terms in addition to the Dirac mass terms in

the SM Lagrangian as follows

$$\begin{aligned}
\mathcal{L}_{\nu_R} &= i\bar{\nu}_R \not{\partial} \nu_R - (\bar{\ell}_L Y_\nu \phi_c \nu_R + \bar{\nu}_R Y_\nu^\dagger \phi_c^\dagger \ell_L) - \frac{1}{2} \left(\bar{\nu}_R^c M_M \nu_R + \bar{\nu}_R M_M^\dagger \nu_R^c \right) \\
&= i\bar{\nu}_R \not{\partial} \nu_R - (\bar{\nu}_L M_\nu \nu_R + \bar{\nu}_R M_\nu^\dagger \nu_L) - \frac{1}{2} \left(\bar{\nu}_R^c M_M \nu_R + \bar{\nu}_R M_M^\dagger \nu_R^c \right) \\
&= i\bar{\nu}_R \not{\partial} \nu_R - \frac{1}{2} \left[\begin{pmatrix} \bar{\nu}_L & \bar{\nu}_R^c \end{pmatrix} \begin{pmatrix} 0 & M_\nu \\ M_\nu^T & M_M \end{pmatrix} \begin{pmatrix} \nu_L^c \\ \nu_R \end{pmatrix} + h.c. \right], \tag{2.13}
\end{aligned}$$

where ν_R^c are the charge conjugates of the right-handed neutrinos, $h.c.$ stands for hermitian conjugate, and Y_ν , M_ν , and M_M are the Yukawa, Dirac mass, and Majorana mass matrices for the neutrinos, respectively.

In the limit $M_M \gg M_\nu$, the combined mass matrix has two distinct sets of eigenvalues: the sterile neutrinos ν_s with masses $m_s \simeq M_M$ and the active neutrinos ν_a with masses $m_a \simeq M_\nu^2/M_M$. The active and sterile neutrinos are related to the left- and right-handed neutrinos by the active-sterile mixing matrix $\theta = M_\nu M_M^{-1}$ as follows

$$\begin{aligned}
|\nu_a\rangle &= \cos \theta |\nu_L\rangle + \sin \theta |\nu_R\rangle \\
|\nu_s\rangle &= -\sin \theta |\nu_L\rangle + \cos \theta |\nu_R\rangle. \tag{2.14}
\end{aligned}$$

In this formulation, the active neutrinos are the observed neutrinos of the SM while the sterile neutrino states are a promising dark matter candidate as they only interact with the SM through neutrino oscillations. Furthermore, the sterile neutrinos must have $m_s \simeq$ keV or else they cannot account for the observed masses of DM-dominated objects without violating the Pauli exclusion principle. Fortunately, this constraint also means that the oscillation rate into active neutrinos is low enough that the sterile neutrino lifetime is longer than the age of the universe. Additionally, the Majorana mass term allows for additional CP-violating phases beyond the Dirac phases discussed in Section 1.6. Astrophysical detection, accelerator production, and neutrinoless double β decay experiments all place constraints on sterile neutrino properties.

2.4 Simplified Models for LHC

Without loss of generality, we assume that dark matter consists of a single Dirac fermion WIMP species χ with mass m_{DM} . In order to observe DM at a hadron collider, there must exist a new mediator particle with mass M_{med} that couples to both SM quarks and χ with couplings g_q and g_{DM} , respectively. In general, this mediator can have any spin structure; for purposes of simplicity, we limit ourselves to the observed mediators in the SM: a spin-0 scalar S , a spin-0 pseudoscalar P , a spin-1 vector V_μ , and a spin-1 axial-vector A_μ (not to be confused with SM photon).

The Lagrangians for these possible mediators are

$$\mathcal{L}_S = \frac{1}{2}M_{\text{med}}^2 S^2 + g_{\text{DM}} \bar{\chi} S \chi + g_q \sum_q \bar{q} Y_q S q \quad (2.15)$$

$$\mathcal{L}_P = \frac{1}{2}M_{\text{med}}^2 P^2 + g_{\text{DM}} \bar{\chi} \gamma^5 P \chi + i g_q \sum_q \bar{q} Y_q \gamma^5 P q \quad (2.16)$$

$$\mathcal{L}_V = \frac{1}{2}M_{\text{med}}^2 V_\mu V^\mu + g_{\text{DM}} \bar{\chi} \not{V} \chi + g_q \sum_q \bar{q} \not{V} q \quad (2.17)$$

$$\mathcal{L}_A = \frac{1}{2}M_{\text{med}}^2 A_\mu A^\mu + g_{\text{DM}} \bar{\chi} \gamma^5 \not{A} \chi + g_q \sum_q \bar{q} \gamma^5 \not{A} q, \quad (2.18)$$

where $\{q\}$ and $\{Y_q\}$ are the SM quarks and their associated Yukawa couplings and we have assumed that the coupling g_q is universal to all quarks without any loss of generality. The width of the mediators is determined by the coupling constants and mass of the mediator. Thus, these four models are described by only four parameters in addition to the spin structure of their couplings: $\{g_q, g_{\text{DM}}, m_{\text{DM}}, M_{\text{med}}\}$. For the results shown in this thesis, we fix $g_q = 0.25$ and $g_{\text{DM}} = 1$ to satisfy the narrow width approximation and provide complimentarity to dijet and dilepton searches for new mediators. Meanwhile, we scan the mass parameters m_{DM} and M_{med} between 1-1000 GeV and 10-2000 GeV, respectively.

As the CMS detector is focused on observing particles through electromagnetic and strong interactions (see Chapter ??), the production of DM particles alone does not result in an observable signature in the detector. Instead, we look for events where

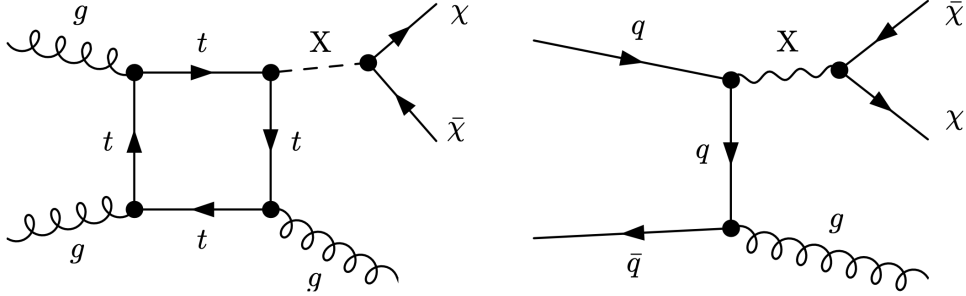


Figure 2-6: Feynmann diagrams for possible dark matter production modes at the LHC, with X denoting the mediator and χ the dark matter particle. The left diagram is most common for scalar and pseudoscalar mediators, while the right diagram is most common for vector and axial mediators. For the right diagram, the gluon can be replaced with any of the EWK gauge boson whereas for the left diagram, other production modes dominate for the EWK gauge bosons. Reprinted from Reference [1].

they are produced in association with a visible SM particle with the resulting signature of the SM particle recoiling against an invisible state. The standard mechanism for producing this final state is for one of the incoming partons to radiate the visible SM particle, usually a quark or a gauge boson, as shown in Figure 2-6. The possible final states split into the categories shown in Table 2.1 with unique final states and interaction strengths.

Table 2.1: Final states of DM production with approximate interaction strength.

Name	Strength	Final State
Monojet	$\mathcal{O}(\alpha_s)$	$j + \chi\bar{\chi}$
Monophoton	$\mathcal{O}(\alpha)$	$\gamma + \chi\bar{\chi}$
Mono-Z	$\mathcal{O}(\alpha)/M_Z^2$	$\ell\ell + \chi\bar{\chi}$

The monojet final state has the highest production rate but also the largest amount of background from SM processes. The Mono-Z final state is the cleanest signature but also has a substantially suppressed production rate due to the mass of the Z boson and the small branching ratio to leptons. The monophoton final state lands in the middle on both metrics: the production rate is $\sim 1/10$ that of the monojet final state but also has fewer backgrounds from SM processes. Additionally, the monophoton state has the “advantage” of being able to distinguish between the spin-0 and spin-1 mediators by the “virtue” of the $gg \rightarrow S\gamma$ and $gg \rightarrow P\gamma$ processes being forbidden by

Furry's theorem. For the bulk of this thesis, we focus on the monophoton final state, saving comparisons against the monojet and mono- Z states for Chapter ??.

2.5 Non-collider Searches

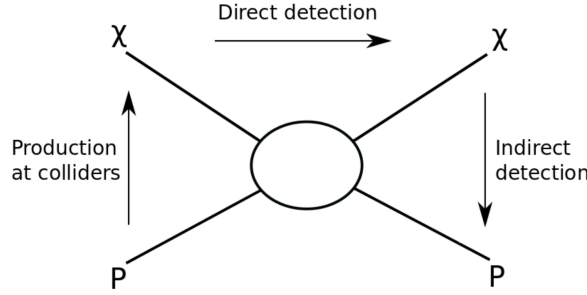


Figure 2-7: Possible dark matter detection channels. Reprinted from Reference [].

The goal of a collider-based search for dark matter is to create pairs of DM candidates through quark-antiquark annihilation, i.e. $q\bar{q} \rightarrow \chi\bar{\chi}$. However, there are other ways you can look at this interaction when attempting to find dark matter, as shown in Figure 2-7. The longest running searches for DM particles have been direct detection searches, where one attempts to observe the scattering of a DM particle off of a heavy nucleus, i.e. $q\chi \rightarrow q\chi$. Another method involves the inverse process utilized at hadron colliders, the observation of SM particles produced in the annihilation of astrophysical DM pairs, i.e. $\chi\bar{\chi} \rightarrow q\bar{q}$. In this section, we shall give a brief overview of the leading experiments for these two approaches.

2.5.1 Direct Detection

Direct detection experiments aim to observe a collision between a DM particle χ and an atomic nucleus N . The typical nuclear recoil for such a collision is in the 1–100 keV range and there are various different technologies that are used to identify the recoiling nucleus, as shown in Figure 2-8. The three main signals are light from a scintillating material, charge from an ionization reaction, and phonons from thermal

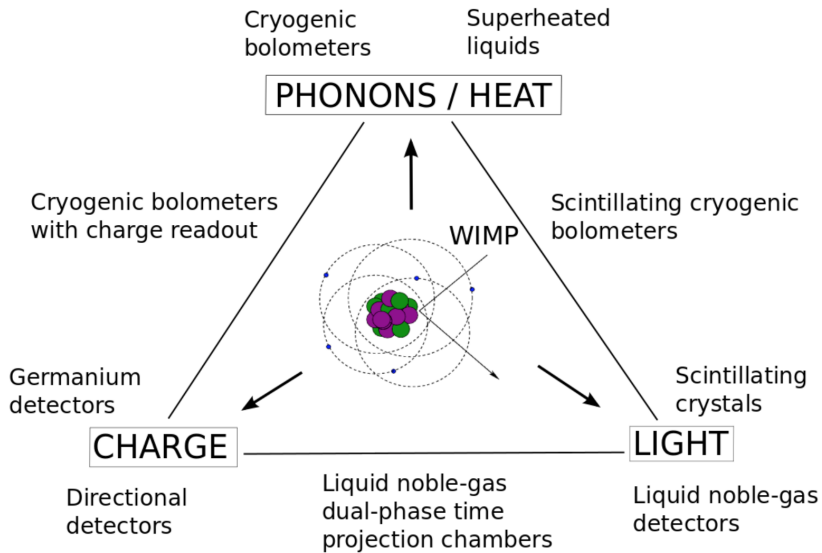


Figure 2-8: Possible signals measured and technologies used in direct detection experiments. Reprinted from Reference [1].

excitations. Many detectors utilize multiple signals in order to enhance background rejection. A final consideration is whether the interaction is spin-independent (SI) or spin-dependent (SD), corresponding to a vector/scalar or axial/pseudoscalar mediator, respectively. The SI DM-nucleus cross-section scales as the number of nucleons squared and thus experiments focusing on SI interactions use materials with a large atomic number. Conversely, the spin-dependent DM-nucleus cross-section depends on the total nuclear spin and experiments focusing on SD interactions use materials with an odd number of nucleons, particularly those with unpaired protons and neutrons. The remainder of this section will discuss three proto-typical direct detection experiments.

The Large Underground Xenon (LUX) experiment is a dual-phase xenon time projection chamber that utilizes both scintillation light and free electrons from ionization to detect nuclear recoils. The active detector volume has 250 kg of ultrapure liquid xenon, a large enough volume that the detector is self-shielding. Odd isotopes make up 47% of naturally occurring xenon, enabling measurements of spin-dependent interactions with approximately half the active detector volume. The latest LUX

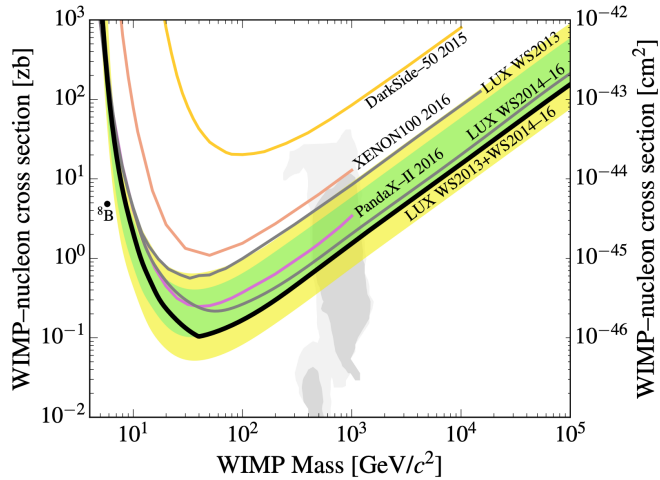


Figure 2-9: Latest SI independent results from the LUX experiment (brazilian flag bands). Reprinted from Reference [1].

results are shown in Figure 2-9.

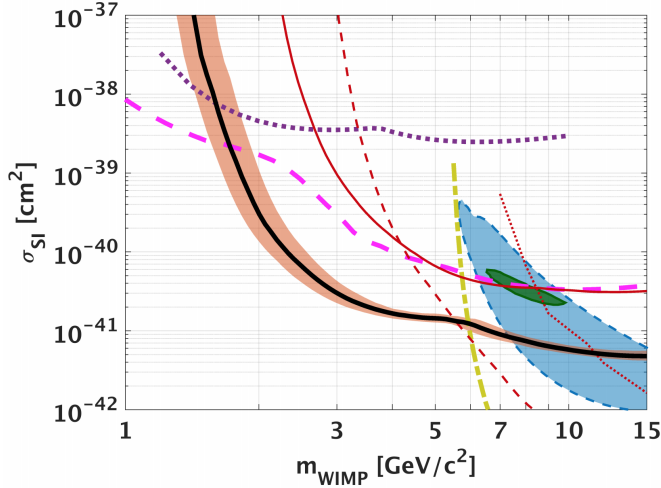


Figure 2-10: Latest SI independent results from the CDMSlite experiment (black line with salmon band). Reprinted from Reference [1].

The CDMSlite experiment uses a cryogenic germanium bolometer that detects phonons and ionization from nuclear recoils. The presence of both signals allows for particle identification, but the most sensitive results only use the phonon signals. CDMSlite is most sensitive to dark matter with masses between 1-10 GeV as shown in Figure 2-10.

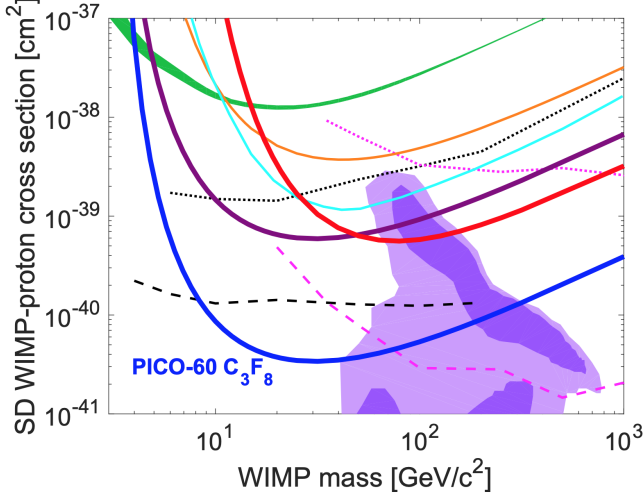


Figure 2-11: Latest SD independent results from the PICO-60 experiment (thick blue line). Reprinted from Reference [].

The PICO-60 experiment uses a bubble chamber filled with C_3F_8 to observe nuclear recoils with a threshold of 13.6 keV. This threshold is high enough to reject backgrounds from minimum ionizing particles while still having sufficient signal efficiency. Furthermore, flourine has exactly one unpaired proton and no unpaired neutrons, greatly enhancing the sensitivity to the proton-coupling SD interactions. The latest results from PICO-60 are shown in Figure 2-11.

2.5.2 Indirect Detection

In Section 2.2, we discussed the process of dark matter annihilation in the early universe and found that the relic density $\Omega_\chi \cdot h^2$ depended on the average annihilation cross section $\langle \sigma_A v \rangle$. In Section 2.3.1, we found that a 100 GeV WIMP particle must have $\langle \sigma_A v \rangle \sim 10^{-26} \text{ cm}^3 \text{ s}^{-1}$ in order to produce the observed relic density. While our calculation in Section 2.2 assumed that the DM number density didn't change appreciably after freezeout, there is still a non-zero annihilation rate of $n_\chi^2 \langle \sigma_A v \rangle / 2$ for dark matter to SM particles. With this decay rate and the observed relic density, there should be $\mathcal{O}(10)$ particles from DM annihilation reaching Earth per year per square meter. Thus, it is possible to learn about dark matter by observing the particle flux near Earth.

While dark matter can decay to a pair of any SM particles, the only ones that live long enough to reach Earth are photons, neutrinos, electrons, positrons, protons, and anti-protons, whether produced directly or from decays of short-lived particles. While it is possible to measure the flux of all of these particles, it is only possible to observe the energy spectrum and source locations of photons and neutrinos as galactic magnetic fields obscure these for the charge particles. Thus, experiments such as the Alpha Magnetic Spectrometer (AMS-02) look for a rise in the positron and anti-proton fractions of the cosmic ray flux to find signs of WIMP annihilation. Similarly, gamma ray telescopes such as the Fermi Large Area Telescope (Fermi-LAT) search for high-energy photons originating from dwarf spheroidal galaxies as they have especially high ratios of dark matter to luminous matter. Both experiments have tentative signals that are yet to be confirmed.

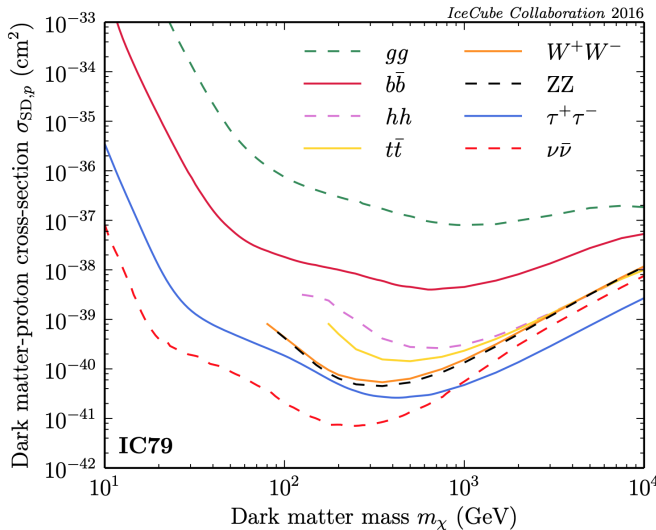


Figure 2-12: Latest SD independent results from the IceCube experiment. Reprinted from Reference [1].

The neutrino channel differs from the other two because it is sensitive to the annihilation of WIMPs that have been gravitationally captured by the sun. While solar WIMPs can decay to any SM particle, only neutrinos are capable of escaping the sun. Furthermore, astrophysical uncertainties are very small for neutrinos originating from the sun versus galactic sources. Additionally, solar WIMPs are in equilibrium, so the annihilation flux depends on the DM-nucleon cross-section instead of the annil-

ihilation cross-section allowing for easy comparison with direct detection experiments. Since the sun consists primarily of hydrogen, observations of solar WIMPs are especially sensitive to spin-dependent processes. The IceCube neutrino observatory is a Cherenkov light detector consisting of a cubic kilometer of Antarctic ice instrumented with 79 strings of photomultiplier tubes. Figure 2-12 shows the latest results from IceCube, with each curves assuming annihilation into a different SM particle pair.

2.6 Summary

Copious astrophysical evidence exists for a non-relativistic non-baryonic type of matter referred to as dark matter that constitutes ~ 27 of the energy of the universe. The favored source for dark matter is a new beyond the Standard Model particle that has weak interactions with photons, baryons, and itself and a relic density of $\Omega_\chi \cdot h^2 = 0.1200 \pm 0.0012$. While other candidates exist, a new weakly-interacting massive particle is a dark matter candidate found in many theories of new physics. Collider, direct detection, and indirect detection searches can all be interpreted in the context of simplified models, which posit a new Dirac fermion DM particle and a massive mediator. The remainder of this thesis focuses on a search for dark matter produced in conjunction with a single photon at the Large Hadron Collider using the Compact Muon Solenoid detector.